$O_2(^1\Delta)$ production in He/O_2 mixtures in flowing low pressure plasmas

D. Shane Stafford[a)]
Department of Chemical and Biomolecular Engineering, University of Illinois, 1406 West Green Street, Urbana, Illinois 61801

Mark J. Kushner[b)]
Department of Electrical and Computer Engineering, University of Illinois, 1406 West Green Street, Urbana, Illinois 61801

(Received 13 February 2004; accepted 11 May 2004)

Chemical oxygen-iodine lasers (COIL) are attractive for diverse industrial applications because they are capable of high efficiency, high power operation, and because the 1.315 μm wavelength can be transmitted through fiber optics and couples efficiently with most metals. Conventional COILs are pumped with $O_2(^1\Delta)$ that is generated by reaction of Cl_2 in a basic H_2O_2 solution. Current trends in pumping COILs involve producing the $O_2(^1\Delta)$ in electric discharges, thereby circumventing the hazards, complexity, and weight associated with pumping and storing caustic liquids. In this work, we have investigated the scaling of $O_2(^1\Delta)$ yields with specific energy deposition in He/O_2 mixtures in flowing radio frequency (rf) discharges at pressures of a few to tens of Torr using a global plasma kinetics model. We found that $O_2(^1\Delta)$ yield increases nearly linearly with specific energy deposition in O_2 molecules up to a few eV per molecule, with yields peaking around 30% by 5–8 eV. Further increases in specific energy deposition serve only to increase O_2 dissociation and gas heating, thereby reducing the $O_2(^1\Delta)$ yield. We also found that variations in peak yields at a given specific energy deposition are caused by secondary effects resulting from dilution, pressure, and power level. We show that these secondary effects alter the $O_2(^1\Delta)$ yield by shifting the $O_2(^1\Sigma)/O_2(^1\Delta)$ ratio.
 [DOI: 10.1063/1.1768615]

I. INTRODUCTION

Chemical laser operation on the $^2P_{1/2} \rightarrow {}^2P_{3/2}$ transition in atomic iodine has been investigated due to its high efficiency and potential for multikilowatt cw power.[1–6] The conventional chemical oxygen-iodine laser (COIL) dissociates I_2 by collisions with $O_2(^1\Delta)$. Subsequent collisions with $O_2(^1\Delta)$ then excite the atomic iodine in a near resonant transfer to create a population inversion and lasing on the $I(^2P_{1/2}) \rightarrow I(^2P_{3/2})$ transition. In order to achieve the flow rates and temperatures required for high power applications, the gas stream is often expanded through a supersonic nozzle. Conventional COILs generate the $O_2(^1\Delta)$ metastable with yields up to 0.7 using liquid phase chemistry by reaction of Cl_2 in basic H_2O_2.[7] This method is less than optimum for some applications because of the complexity, weight, and operational hazards associated with the liquid chemical storage and pumping systems. Therefore, recent efforts have been investigating the development of all gas phase $O_2(^1\Delta)$ generators.[8,9]

Current research in gas phase $O_2(^1\Delta)$ generation involves capacitive, inductive, and microwave self-sustaining electric discharges in pure O_2 and in mixtures with diluents such as N_2 and He, and *e*-beam non-self-sustained discharges in similar mixtures.[10–16] The threshold $[O_2(^1\Delta)]/[O_2(^3\Sigma)]$ ratio required for positive laser gain for conventional systems depends on the cavity temperature and can be derived from the equilibrium of the forward and reverse rates of the pumping reaction,[17]

$$\frac{[O_2(^1\Delta)]}{[O_2(^3\Sigma)]} = 0.67 \exp\left(-\frac{401.4}{T}\right), \tag{1}$$

where the temperature T has units K. At room temperature the threshold ratio is 0.18. Early attempts by Benard and Pchelkin using a microwave discharge as a source of $O_2(^1\Delta)$ produced $[O_2(^1\Delta)]/[O_2(^3\Sigma)]$ fractions of 0.11.[18] Later, Fournier *et al.* proposed that the maximum achievable excitation fraction in a discharge is 0.135, based on excitation equilibrium calculations and experiments using an electron-beam sustained discharge at 1.15 bars.[19]

More recent investigations on electric discharge production of $O_2(^1\Delta)$ have centered on engineering the reduced electric field (E/N) nearer to the optimum value for $O_2(^1\Delta)$ production which, based on calculations of the electron energy distribution for discharges in pure O_2, is $\approx$10 Td (1 Td=10^{-17} V cm^2).[11,14,20,21] This value is too low for self-sustained discharges. In an attempt to circumvent the loss of efficiency of $O_2(^1\Delta)$ excitation that occurs in self-sustained discharges, Hill developed a controlled avalanche discharge in which short, high voltage pulses ionize the gas while a lower electric field sustains the discharge between the pulses.[10] This method has been used by Hill to obtain 0.16 yield and has also been investigated by Verdeyen *et al.*[22]

Electron beam sustained discharges have also been investigated by Ionin *et al.*[14] With the addition of Ar and CO or H_2 to the O_2, they were able to increase the specific en-

a)Electronic mail: dstaffor@uiuc.edu
b)Author to whom correspondence should be addressed; electronic mail: mjk@uiuc.edu

ergy input obtainable with an *e*-beam up to about 1.5 eV per molecular component. Their modeling results for non-self-sustained discharges predicted yields up to 0.25 with $O_2(^1\Delta)$ excitation efficiencies of ≈0.4 when using molecular additives such as CO, H_2, or D_2. Inert gas diluents and molecular additives have also been used with success by Schmiedberger with a hollow cathode radio frequency (rf) jet discharge.[12] At 0.43 Torr, a 0.32 yield was obtained by flowing an $O_2/N_2/NO$ mixture through the discharge jet and then chilling the gas by mixing with a cold Ar/NO_2 stream. However, the pressure was lower than typical high power COIL system pressures.

Moderate yields at higher pressures have been recently achieved by Rakhimova *et al.* and Savin *et al.*[15,16] Rakhimova *et al.* performed experiments in a transverse electrode capacitive discharge in pure O_2 and in mixtures with Ar and He from 1 to 40 Torr.[15] They obtained an $[O_2(^1\Delta)]/[O_2(^3\Sigma)]$ ratio of 0.3 in pure O_2 and 0.4 in mixtures with He and Ar which showed good agreement with a numerical model. Savin *et al.* obtained 0.25–0.30 yield in 1–2 Torr of pure O_2 in a traveling microwave discharge, also obtaining good agreement with a model.[16] Both of these kinetic models include a three-body $O_2(^1\Delta)$ quenching reaction proposed by Ivanov,[11,15,16]

$$O + O_2(^1\Delta) + O_2 \rightarrow O + O_2 + O_2, \quad k = 10^{-32}\ \text{cm}^6\ \text{s}^{-1}. \tag{2}$$

In this paper, we present results from a computational investigation of $O_2(^1\Delta)$ yields produced by self-sustained discharges in He/O_2 mixtures. A global plasma kinetics model was modified to address one-dimensional steady-state plug flow and was validated against experiments. The effects of typical discharge variables—mixture, pressure, flow rate, and power—were investigated. We found that yields of $O_2(^1\Delta)$ increase linearly with O_2 specific energy deposition up to a saturation regime at 5–8 eV per molecule before decreasing again as O_2 dissociation begins to dominate the kinetics. We also found that the dissociation fraction reaches 0.5 when the peak $O_2(^1\Delta)$ yield occurs. The dissociation fraction increases monotonically with specific energy deposition, exceeding 0.9 by 20 eV per molecule. However, after correcting for specific energy deposition, the peak yield in the saturation regime is still influenced by composition, power deposition, and pressure. Moderate changes in these parameters cause up to a 50% variation in the peak yield at a given energy deposition. We found that the variations in yield are caused by changes in gas density and mole fractions which affect the $O_2(^1\Delta)$ and $O_2(^1\Sigma)$ kinetics and that the variations are largely independent of E/N.

The plasma kinetics model used in this investigation, GlobalKin, is described in Sec. II. The gas phase and electron impact reaction kinetics are discussed in Sec. III. Scaling of $O_2(^1\Delta)$ yield is discussed in Sec. IV. Concluding remarks are in Sec. V.

II. DESCRIPTION OF THE MODEL

A schematic of a typical electrical discharge COIL device is shown in Fig. 1. Oxygen and a diluent such as He are

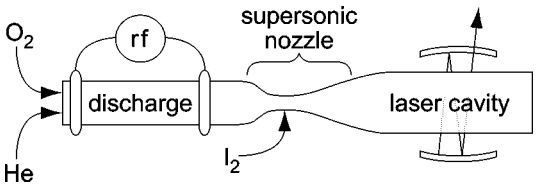

FIG. 1. Schematic of typical electric discharge COIL. O_2 is mixed with an inert gas and flowed through the discharge. The gases are then cooled by supersonic expansion before entering the laser cavity.

first fed through a quartz tube, where the plasma is sustained by a capacitive or inductive discharge. Powers of tens to hundreds W are deposited into gases flowing at hundreds to thousands cm/s. Pressures are a few to tens of Torr for O_2 mixtures with mole fractions of 0.03–1 with the balance an inert gas diluent. The gases may be precooled before entering the discharge but usually enter at about 300 K. The discharge section is usually a few tens of centimeter in length and a few centimeters in diameter. Following the plasma, the excited oxygen and diluent are fed through a nozzle where I_2 is injected into the flow. To aid in I_2 mixing the I_2 secondary flow is typically injected tangentially to the primary flow in the subsonic portion of a supersonic nozzle. The gases then mix, react and cool as they flow through the transonic and supersonic portions of the nozzle. Ideally the gases are cooled to around 140 K as they flow through the laser cavity and are drawn into the exhaust system.[23]

GlobalKin, a global plasma kinetics model,[24] was modified to simulate steady-state plug flow for this investigation. GlobalKin consists of three main modules: a reaction chemistry and transport module, a Boltzmann equation solver for the electron energy distribution (EED), and an ordinary differential equation (ODE) solver module. The reaction chemistry and transport module constructs differential equations for the time evolution of species densities and temperatures using results obtained by the Boltzmann solver for electron impact rate coefficients. The differential equations are then integrated by the stiff ODE solver.[25]

The chemistry and transport module first constructs continuity equations for neutral [Eq. (3)] and charged [Eq. (4)] species, accounting for diffusion to and from the walls and reaction sources,

$$\frac{dN_i}{dt} = -\nabla \cdot \left(-\nabla (D_i N_i) + \sum_j \nabla \cdot (D_j N_j) \gamma_j f_{ji} \right) + S_i - \frac{N_i}{T_g}\frac{dT_g}{dt}, \tag{3}$$

$$\frac{dN_i^{\pm}}{dt} = -\nabla \cdot [-\nabla (D_{a,i} N_i)] + S_i, \tag{4}$$

where N_i and $N_i^{\pm}$ are the densities of neutral and charged species i, D_i and $D_{a,i}$ are the regular and ambipolar diffusivities of species i in the mixture, and the sum is over all species. γ_j is the wall reactive sticking coefficient of species j, f_{ji} is the returned fraction of species j as species i from the wall, and S_i is the reaction source term for species i. The last term accounts for excursions of the gas temperature T_g as-

suming constant pressure operation. The diffusivities are estimated from Lennard-Jones potentials and are calculated for each species as a function of the local gas composition. The ambipolar diffusion coefficients for charged species are based on the instantaneous ion and electron mobilities and diffusivities. Ion mobilities are obtained from experimental databases[26–29] or estimated based on Langevin values. The electron mobility is obtained from the EED.

For the spatially uniform volumetric model, the second-order partial derivatives in the continuity equations can be approximated by substituting the diffusion length Λ, and simplify to

$$\frac{dN_i}{dt} = \frac{1}{\Lambda^2}\left(-D_i N_i + \sum_j D_j N_j \gamma_j f_{ji}\right) + S_i - \frac{N_i}{T_g}\frac{dT_g}{dt}. \tag{5}$$

The source terms for the gas phase and electron impact reactions are obtained from rate expressions for all species,

$$S_i = \sum_j (a_{ij}^{\mathrm{RHS}} - a_{ij}^{\mathrm{LHS}}) k_j \prod_l N_l^{a_{ij}^{(\mathrm{LHS})}}, \tag{6}$$

where the a_{ij} are the stoichiometric coefficients of species i in reaction j on the right-hand side (RHS) and left-hand side (LHS), k_j is the reaction rate coefficient for reaction j, and the product is over all LHS species in reaction j. Rate coefficients are obtained from Arrenhius expressions for the gas phase reactions and from the EED for the electron impact reactions.

For the relatively high pressures (1–100 Torr) typical of COIL discharges, the ions and neutrals are in near thermal equilibrium and can be described by a single temperature. The energy conservation equation for the heavy species includes terms for contributions to gas heating from elastic and inelastic collisions with electrons, from gas phase reaction sources, and from conduction to the walls,

$$\frac{d}{dt}(N c_P T_g) = \sum_i \frac{3}{2} n_e \nu_{mi}\left(\frac{2m_e}{M_i}\right) k_B (T_e - T_g) + \sum_j n_e k_j N_j \Delta\varepsilon_j - \sum_j \Delta H_j + \frac{\kappa}{\Lambda^2}(T_w - T_g) - \frac{d}{dt}\left(\frac{1}{2} M_w N v_x^2\right), \tag{7}$$

where N is the total gas density and c_P is the mixture averaged heat capacity. ν_{mi} is the momentum transfer collision frequency between electrons and species i, m_e is the electron mass, M_i is the mass of species i, k_B is the Boltzmann constant, T_e is the average electron energy, k_j and $\Delta\varepsilon_j$ are the rate constant and energy contribution from inelastic process j, and ΔH_j is the heat of reaction for process j. The second to last term represents conduction to the wall, where κ is the mixture averaged thermal conductivity and T_w is the wall temperature. The mixture averaged heat capacity and thermal conductivity are estimated from the Lennard-Jones potentials. For some of the most prevalent species in the discharge [He, O_2, and $O_2(^1\Delta)$], the heat capacities are obtained from polynomial correlations for greater accuracy.[30] The last term of Eq. (7) accounts for the transfer of internal energy to kinetic energy as the gas expands and the flow velocity v_x increases. In this term, M_w is the mixture averaged molecular weight.

Energy conservation for electrons includes contributions from Joule heating and energy transferred in elastic and inelastic collisions with heavy species,

$$\frac{d}{dt}\left(\frac{3}{2} n_e k_B T_e\right) = P_d - \sum_i \frac{3}{2} n_e \nu_{mi}\left(\frac{2m_e}{M_i}\right) k_B (T_e - T_g) + \sum_l n_e k_l N_l \Delta\varepsilon_l, \tag{8}$$

where P_d is the power deposition. In a plug flow model, a circuit parameter (e.g., current density or power) must be specified as a function of distance along the flow direction. We chose to specify power deposition. When used in this manner, P_d represents the time-averaged power deposition into the electrons over multiple rf cycles. In this regard, the discharge kinetics are analogous to a dc positive column model or inductive discharge with an axially varying E/N as might occur when conductivity is a function of position.

The electron transport coefficients required for Eqs. (4)–(8) are generated by solving Boltzmann's equation for the EED. The Boltzmann solver is invoked at specified intervals during the simulation to reflect changes in the composition of the gas mixture. The EED is obtained by iterative solution of the two-term spherical harmonic expansion of the Boltzmann equation.[31] The Boltzmann module tabulates average electron energies, transport coefficients, and rate constants for a range of values of E/N and the results are exported to GlobalKin. GlobalKin then interpolates from the tables based on the instantaneous average electron energy obtained by integrating Eq. (8) to obtain electron impact reaction rate coefficients and the E/N required to produce the derived average electron energy.

In order to address the flow conditions of the COIL system, the global model was converted to a pseudo-one-dimensional plug flow model by introducing the flow velocity v_x and by accounting for gas expansion at constant pressure [Eqs. (3) and (5)]. The change in flow speed is obtained by conservation of mass flux,

$$\frac{dv_x}{dt} = -\frac{v_x}{\rho}\frac{d\rho}{dt}, \tag{9}$$

where the mass density ρ is obtained from the instantaneous mixture averaged molecular weight M_w and the number density N. Integrating the flow velocity gives the location of the initial gas plug as a function of time.

The resulting ordinary differential equations for species densities [Eqs. (3) and (4)], gas and electron energy [Eqs. (7) and (8)], and flow velocity [Eq. (9)] are normalized in GlobalKin to increase computational efficiency before being integrated. Integration is performed by a double precision variable-coefficient ODE solver developed at LLNL as part of ODEPACK.[25]

III. REACTION MECHANISM

The mechanism used in this investigation involves reactions in the gas phase discharge and afterglow as well as

recombination and quenching reactions on the discharge tube walls. The species in the mechanism include ground state neutrals O_2, O, O_3, and He; vibrational and electronic states $O_2(v)$, $O_2(a^1\Delta)$, $O_2(b^1\Sigma)$, $O(^1D)$, $O(^1S)$, and $He(^2S)$; and ions O_2^+, O^+, He^+, O_2^-, O^-, and O_3^-. [$O_2(v)$ represents the total vibrational population consisting of the first four vibrational levels of O_2.] The complete gas phase reaction mechanism is shown in Table I. Wall reactions are listed in Table II. Typical densities and temperatures are shown in Fig. 2 (to be discussed in full below).

Electron impact reactions dominate the kinetics in the discharge region. At the discharge inlet, where only ground state O_2 and He are present, the O_2 is excited and dissociated, mainly by the four reactions,

$$e + O_2 \rightarrow O_2(^1\Delta) + e, \tag{10}$$

$$e + O_2 \rightarrow O(^1D) + O + e, \tag{11}$$

$$e + O_2 \rightarrow O + O + e, \tag{12}$$

$$e + O_2 \rightarrow O_2(^1\Sigma) + e. \tag{13}$$

In the first section of the discharge, most of the $O_2(^1\Delta)$ is produced by direct electron impact [Eq. (10)]. However, the rates of the dissociation reactions [Eqs. (11) and (12)] are also large in the discharge, producing large densities of O atoms. These atoms are then excited to $O(^1D)$ by electron impact, thereby creating more $O_2(^1\Delta)$ through a sequence of collisions with O_2,

$$O(^1D) + O_2 \rightarrow O + O_2(^1\Sigma),$$

$$k = 2.0 \times 10^{-1}\ \text{cm}^3\ \text{s}^{-1} \quad \text{(Ref. 32)}, \tag{14}$$

$$O + O_2(^1\Sigma) \rightarrow O + O_2(^1\Delta),$$

$$k = 7.2 \times 10^{-14}\ \text{cm}^3\ \text{s}^{-1} \quad \text{(Ref. 32)}, \tag{15}$$

where k is the rate coefficient at 300 K.

As the $O_2(^1\Delta)$ density increases in the downstream portion of the discharge, processes which remove $O_2(^1\Delta)$ through excitation to upper states, through dissociation, and through superelastic deexcitation to the ground state begin to dominate the kinetics,

$$e + O_2(^1\Delta) \rightarrow O_2(^1\Sigma) + e, \tag{16}$$

$$e + O_2(^1\Delta) \rightarrow O(^1D) + O + e, \tag{17}$$

$$e + O_2(^1\Delta) \rightarrow O + O + e, \tag{18}$$

$$e + O_2(^1\Delta) \rightarrow O_2 + e. \tag{19}$$

These processes produce more long lived O atoms and deplete the O_2 available for excitation to $O_2(^1\Delta)$. In this downstream region the discharge becomes less efficient at producing $O_2(^1\Delta)$, and atomic O is produced instead.

Ozone is also created early in the discharge, primarily through collisions of $O_2(^1\Delta)$ and O^- ions and through a three-body reaction,

$$O^- + O_2(^1\Delta) \rightarrow O_3 + e,$$

TABLE I. Discharge and afterglow reaction mechanism for He/O_2.

Reaction	Rate constant[a,b]	Reference
$e+He \rightarrow He^*+e$	$f(T_e)$	39
$e+He \rightarrow He^*+e$	$f(T_e)$	39
$e+He \rightarrow He^++e+e$	$f(T_e)$	40
$e+He^* \rightarrow He^++e+e$	$f(T_e)$	41
$e+He^* \rightarrow He+e$	$f(T_e)$	c
$e+He^+ \rightarrow He^*$	$6.76\times10^{-13}T_e^{-0.5}$	42
$e+e+He^+ \rightarrow He^*+e$	$5.12\times10^{-27}T_e^{-4.5}$	42
$e+O_2 \rightarrow O^-+O$	$f(T_e)$	43
$e+O_2 \rightarrow O_2(v)+e$	$f(T_e)$	43
$e+O_2 \rightarrow O_2(v)+e$	$f(T_e)$	43
$e+O_2 \rightarrow O_2(v)+e$	$f(T_e)$	43
$e+O_2 \rightarrow O_2(v)+e$	$f(T_e)$	43
$e+O_2 \rightarrow O_2(^1\Delta)+e$	$f(T_e)$	43
$e+O_2 \rightarrow O_2(^1\Sigma)+e$	$f(T_e)$	43
$e+O_2 \rightarrow O+O+e$	$f(T_e)$	43
$e+O_2 \rightarrow O(^1D)+O+e$	$f(T_e)$	43
$e+O_2 \rightarrow O_2^++e+e$	$f(T_e)$	43
$e+O_2 \rightarrow O^++O+e+e$	$f(T_e)$	44
$e+O_2+M \rightarrow O_2^-+M$	$3.60\times10^{-31}T_e^{-0.5}$	45
$e+O_2^+ \rightarrow O+O$	$1.20\times10^{-8}T_e^{-0.7}$	46
$e+O_2^+ \rightarrow O(^1D)+O$	$8.88\times10^{-9}T_e^{-0.7}$	46
$e+O_2(v) \rightarrow O^-+O$	$f(T_e)$	d
$e+O_2(v) \rightarrow O_2+e$	$f(T_e)$	c
$e+O_2(v) \rightarrow O_2(^1\Delta)+e$	$f(T_e)$	e
$e+O_2(v) \rightarrow O_2(^1\Sigma)+e$	$f(T_e)$	e
$e+O_2(v) \rightarrow O+O+e$	$f(T_e)$	e
$e+O_2(v) \rightarrow O(^1D)+O+e$	$f(T_e)$	e
$e+O_2(v) \rightarrow O_2^++e+e$	$f(T_e)$	e
$e+O_2(v) \rightarrow O(^1D)+O(^1D)+e$	$f(T_e)$	e
$e+O_2(v) \rightarrow O^++O+e+e$	$f(T_e)$	e
$e+O_2(^1\Delta) \rightarrow O^-+O$	$f(T_e)$	47
$e+O_2(^1\Delta) \rightarrow O_2(^1\Sigma)+e$	$f(T_e)$	48
$e+O_2(^1\Delta) \rightarrow O_2+e$	$f(T_e)$	c
$e+O_2(^1\Delta) \rightarrow O+O+e$	$f(T_e)$	e
$e+O_2(^1\Delta) \rightarrow O(^1D)+O+e$	$f(T_e)$	e
$e+O_2(^1\Delta) \rightarrow O_2^++e+e$	$f(T_e)$	e
$e+O_2(^1\Delta) \rightarrow O(^1D)+O(^1D)+e$	$f(T_e)$	e
$e+O_2(^1\Delta) \rightarrow O^++O+e+e$	$f(T_e)$	e
$e+O_2(^1\Sigma) \rightarrow O^-+O$	$f(T_e)$	f
$e+O_2(^1\Sigma) \rightarrow O_2(^1\Delta)+e$	$f(T_e)$	g
$e+O_2(^1\Sigma) \rightarrow O_2+e$	$f(T_e)$	c
$e+O_2(^1\Sigma) \rightarrow O+O+e$	$f(T_e)$	e
$e+O_2(^1\Sigma) \rightarrow O(^1D)+O+e$	$f(T_e)$	e
$e+O_2(^1\Sigma) \rightarrow O_2^++e+e$	$f(T_e)$	e
$e+O_2(^1\Sigma) \rightarrow O(^1D)+O(^1D)+e$	$f(T_e)$	e
$e+O_2(^1\Sigma) \rightarrow O^++O+e+e$	$f(T_e)$	e
$e+O_3 \rightarrow O^-+O_2$	$f(T_e)$	49
$e+O_3 \rightarrow O_2^-+O$	$f(T_e)$	49
$e+O \rightarrow O(^1D)+e$	$f(T_e)$	50
$e+O \rightarrow O(^1S)+e$	$f(T_e)$	50
$e+O \rightarrow O^++e+e$	$f(T_e)$	50
$e+O(^1D) \rightarrow O+e$	$f(T_e)$	c
$e+O(^1D) \rightarrow O^++e+e$	$f(T_e)$	h
$e+O(^1S) \rightarrow O+e$	$f(T_e)$	c
$e+O(^1S) \rightarrow O^++e+e$	$6.60\times10^{-9}T_e^{0.6}\exp(-9.43/T_e)$	i
$e+O^- \rightarrow O+e+e$	$1.95\times10^{-12}T_e^{0.5}\exp(-3.4/T_e)$	51
$e+O^+ \rightarrow O(^1D)$	$5.30\times10^{-13}T_e^{-0.5}$	42
$e+e+O^+ \rightarrow O(^1D)+e$	$5.12\times10^{-27}T_e^{-4.5}$	42

TABLE I. (*Continued.*)

Reaction	Rate constant[a,b]	Reference
$O^- + O_2^+ \rightarrow O + O_2$	$2\times10^{-7}T_0^{-1}$	46
$O^- + O_2^+ \rightarrow O + O + O$	1×10^{-7}	46
$O^- + O^+ \rightarrow O + O$	$2\times10^{-7}T_0^{-1}$	46
$O^- + H^+ \rightarrow O + He$	$2\times10^{-7}T_0^{-1}$	46
$O_2^- + O_2^+ \rightarrow O_2 + O_2$	$2\times10^{-7}T_0^{-1}$	46
$O_2^- + O_2^+ \rightarrow O_2 + O + O$	1×10^{-7}	46
$O_2^- + O^+ \rightarrow O_2 + O$	$2\times10^{-7}T_0^{-1}$	46
$O_2^- + He^+ \rightarrow O_2 + He$	$2\times10^{-7}T_0^{-1}$	46
$O_3^- + O_2^+ \rightarrow O_3 + O_2$	$2\times10^{-7}T_0^{-1}$	46
$O_3^- + O_2^+ \rightarrow O_3 + O + O$	1×10^{-7}	46
$O_3^- + O^+ \rightarrow O_3 + O$	$2\times10^{-7}T_0^{-1}$	46
$O_3^- + He^+ \rightarrow O_3 + He$	$2\times10^{-7}T_0^{-1}$	46
$O^- + O_2^+ + M \rightarrow O + O_2 + M$	$2\times10^{-25}T_0^{-2.5}$ cm^6 s^{-1}	46
$O^- + O^+ + M \rightarrow O + O + M$	$2\times10^{-25}T_0^{-2.5}$ cm^6 s^{-1}	46
$O^- + He^+ + M \rightarrow O + He + M$	$2\times10^{-25}T_0^{-2.5}$ cm^6 s^{-1}	46
$O^- + O \rightarrow O_2 + e$	$2\times10^{-10}T_0^{0.5}$	33
$O^- + O_2(^1\Delta) \rightarrow O_3 + e$	$3\times10^{-10}T_0^{0.5}$	33
$O^- + O_2(^1\Sigma) \rightarrow O + O_2 + e$	$6.9\times10^{-10}T_0^{0.5}$	46
$O^- + O_2 \rightarrow O_3 + e$	$5\times10^{-15}T_0^{0.5}$	46
$O^- + O_3 \rightarrow O_2 + O_2 + e$	$3.01\times10^{-10}T_0^{0.5}$	33
$O^- + O_3 \rightarrow O_3^- + O$	$1.99\times10^{-10}T_0^{0.5}$	33
$O^- + O_3 \rightarrow O_2^- + O_2$	$1.02\times10^{-11}T_0^{0.5}$	33
$O_2^- + O \rightarrow O^- + O_2$	$1.5\times10^{-10}T_0^{0.5}$	33
$O_2^- + O \rightarrow O_3 + e$	$1.5\times10^{-10}T_0^{0.5}$	33
$O_2^- + O_2(^1\Delta) \rightarrow e + O_2 + O_2$	$2\times10^{-10}T_0^{0.5}$	33
$O_2^- + O_3 \rightarrow O_3^- + O_2$	$6\times10^{-10}T_0^{0.5}$	33
$O_3^- + O \rightarrow O_2^- + O_2$	$2.5\times10^{-10}T_0^{0.5}$	33
$O + O^+ \rightarrow O + O^+$	$1\times10^{-9}T_0^{0.5}$	j
$O + O^+ + M \rightarrow O_2^+ + M$	$1\times10^{-29}T_0^{0.5}$ cm^6 s^{-1}	46
$O_2 + O_2^+ \rightarrow O_2 + O_2^+$	$1\times10^{-9}T_0^{0.5}$	28
$O^+ + O_2 \rightarrow O_2^+ + O$	$2\times10^{-11}T_0^{-0.4}$	33
$O^+ + O_3 \rightarrow O_2^+ + O_2$	1×10^{-10}	46
$O(^1D) + O \rightarrow O + O$	8×10^{-12}	46
$O(^1D) + O_2 \rightarrow O + O_2(^1\Sigma)$	$2.56\times10^{-11}\exp(-67/T_g)$	32
$O(^1D) + O_2 \rightarrow O + O_2(^1\Delta)$	$1.6\times10^{-12}\exp(-67/T_g)$	32
$O(^1D) + O_2 \rightarrow O + O_2$	$4.8\times10^{-12}\exp(-67/T_g)$	32
$O(^1D) + O_3 \rightarrow O_2 + O + O$	1.2×10^{-10}	37
$O(^1D) + O_3 \rightarrow O_2 + O_2$	1.2×10^{-10}	36
$O(^1D) + He \rightarrow O + He$	1×10^{-13}	52
$O(^1S) + O_2 \rightarrow O(^1D) + O_2$	$3.2\times10^{-12}\exp(-850/T_g)$	36
$O(^1S) + O_2 \rightarrow O + O_2$	$1.6\times10^{-12}\exp(-850/T_g)$	36
$O(^1S) + O_2(^1\Delta) \rightarrow O + O_2$	1.1×10^{-10}	46, k
$O(^1S) + O_2(^1\Delta) \rightarrow O(^1D) + O_2(^1\Sigma)$	2.9×10^{-11}	46
$O(^1S) + O_2(^1\Delta) \rightarrow O + O + O$	3.2×10^{-11}	46
$O(^1S) + O \rightarrow O(^1D) + O$	$1.67\times10^{-11}\exp(-300/T_g)$	36
$O(^1S) + O \rightarrow O + O$	$3.33\times10^{-11}\exp(-300/T_g)$	36
$O(^1S) + O_3 \rightarrow O_2 + O_2$	5.8×10^{-10}	36,1
$O_2(^1\Delta) + O \rightarrow O_2 + O$	2×10^{-16}	36
$O_2(^1\Delta) + O_2 \rightarrow O_2 + O_2$	$3\times10^{-18}\exp(-200/T_g)$	32
$O_2(^1\Delta) + O_2(^1\Delta) \rightarrow O_2 + O_2$	$9\times10^{-17}\exp(-560/T_g)$	36, m
$O_2(^1\Delta) + O_2(^1\Delta) \rightarrow O_2(^1\Sigma) + O_2$	$9\times10^{-17}\exp(-560/T_g)$	m
$O_2(^1\Delta) + O_2 \rightarrow O + O_3$	$2.95\times10^{-21}T_0^{0.5}$	
$O_2(^1\Delta) + O_3 \rightarrow O_2 + O_2 + O$	$5.2\times10^{-11}\exp(-2840/T_g)$	37
$O_2(^1\Delta) + He \rightarrow O_2 + He$	$8\times10^{-21}T_0^{0.5}$	53
$O_2(^1\Sigma) + O_2(^1\Sigma) \rightarrow O_2(^1\Delta) + O_2$	$3.6\times10^{-17}T_0^{0.5}$	32, j

TABLE I. (*Continued.*)

Reaction	Rate constant[a,b]	Reference
$O_2(^1\Sigma) + O_2 \rightarrow O_2(^1\Delta) + O_2$	$3.6\times10^{-17}T_0^{0.5}$	32
$O_2(^1\Sigma) + O_2 \rightarrow O_2 + O_2$	$4\times10^{-18}T_0^{0.5}$	32
$O_2(^1\Sigma) + O \rightarrow O_2(^1\Delta) + O$	$7.2\times10^{-14}T_0^{0.5}$	32
$O_2(^1\Sigma) + O \rightarrow O_2 + O$	$8\times10^{-15}T_0^{0.5}$	32
$O_2(^1\Sigma) + O_3 \rightarrow O + O_2 + O_2$	$7.33\times10^{-12}T_0^{0.5}$	34
$O_2(^1\Sigma) + O_3 \rightarrow O_2(^1\Delta) + O_3$	$7.33\times10^{-12}T_0^{0.5}$	34
$O_2(^1\Sigma) + O_3 \rightarrow O_2 + O_3$	$7.33\times10^{-12}T_0^{0.5}$	34
$O_2(^1\Sigma) + He \rightarrow O_2(^1\Delta) + He$	$1\times10^{-17}T_0^{0.5}$	j
$O_2(v) + O \rightarrow O_2 + O$	$1\times10^{-14}T_0^{0.5}$	32, j
$O_2(v) + O_2 \rightarrow O_2 + O_2$	$1\times10^{-14}T_0^{0.5}$	32, j
$O_2(v) + He \rightarrow O_2 + He$	$1\times10^{-14}T_0^{0.5}$	32, j
$O + O + O_2 \rightarrow O_2 + O_2$	$2.56\times10^{-34}T_0^{-0.63}$ cm^6 s^{-1}	46
$O + O + O \rightarrow O_2 + O$	$9.21\times10^{-34}T_0^{-0.63}$ cm^6 s^{-1}	46
$O + O + He \rightarrow O_2 + He$	1×10^{-33} cm^6 s^{-1}	46,[53]
$O + O + O_2 \rightarrow O_2(^1\Delta) + O_2$	$1.93\times10^{-35}T_0^{-0.63}$ cm^6 s^{-1}	46
$O + O + O \rightarrow O_2(^1\Delta) + O$	$6.93\times10^{-35}T_0^{-0.63}$ cm^6 s^{-1}	46
$O + O + He \rightarrow O_2(^1\Delta) + He$	9.88×10^{-35} cm^6 s^{-1}	46,[53]
$O + O_2 + O_2 \rightarrow O_3 + O_2$	$6\times10^{-34}T_0^{-2.8}$ cm^6 s^{-1}	32
$O + O_2 + He \rightarrow O_3 + He$	$3.4\times10^{-34}T_0^{-1.2}$ cm^6 s^{-1}	53
$O + O_2 + O \rightarrow O_3 + O$	$3.4\times10^{-34}T_0^{-1.2}$ cm^6 s^{-1}	j
$O + O_3 + O_2 \rightarrow O_2$	$8\times10^{-12}\exp(-2060/T_g)$	32
$O_3 + M \rightarrow O_2 + O + M$	$1.56\times10^{-9}\exp(-11,490/T_g)$	54, j
$He^* + He^* \rightarrow He + He^+ + e$	$1.5\times10^{-9}T_0^{0.5}$	55
$He^* + O_2 \rightarrow O_2^+ + He + e$	$2.54\times10^{-10}T_0^{0.5}$	56
$He^* + O_3 \rightarrow O_2^+ + O + He + e$	$2.54\times10^{-10}T_0^{0.5}$	56, n
$He^* + O_2(^1\Sigma) \rightarrow O_2^+ + He + e$	$2.54\times10^{-10}T_0^{0.5}$	56, n
$He^* + O \rightarrow O^+ + He + e$	$2.54\times10^{-10}T_0^{0.5}$	56, n
$He^* + O(^1D) \rightarrow O^+ + He + e$	$2.54\times10^{-10}T_0^{0.5}$	56, n
$He^* + O(^1S) \rightarrow O^+ + He + e$	$2.54\times10^{-10}T_0^{0.5}$	56, n
$He^+ + O_2 \rightarrow O^+ + O + He$	$1.07\times10^{-9}T_0^{0.5}$	33
$He^+ + O_3 \rightarrow O^+ + O_2 + He$	$1.07\times10^{-9}T_0^{0.5}$	n
$He^+ + O_2 \rightarrow O_2^+ + He$	$3.3\times10^{-11}T_0^{0.5}$	33
$He^+ + O_2(^1\Delta) \rightarrow O^+ + O + He$	$1.07\times10^{-9}T_0^{0.5}$	n
$He^+ + O_2(^1\Delta) \rightarrow O_2^+ + He$	$3.3\times10^{-11}T_0^{0.5}$	n
$He^+ + O \rightarrow O^+ + He$	$5\times10^{-11}T_0^{0.5}$	j
$He^+ + O(^1D) \rightarrow O^+ + He$	$5\times10^{-11}T_0^{0.5}$	j
$He^+ + O(^1S) \rightarrow O^+ + He$	$5\times10^{-11}T_0^{0.5}$	j
$He^+ + He^+ \rightarrow He + He^+$	$1\times10^{-9}T_0^{0.5}$	28

[a]Rate coefficients have units of cm^3 s^{-1} unless otherwise noted. $T_0 = (T_g/300)$; T_g has units K; T_e has units eV.

[b]$f(T_e)$ indicates that the rate coefficient is obtained from the EED using cross section from indicated reference. Rate coefficients are compiled as a function of E/N and interpolated based on instantaneous values of T_e.

[c]Superelastic cross section calculated using detailed balance.

[d]Estimated to have the same cross section as the ground state reaction.

[e]Cross section estimated by shifting and scaling the ground state cross section by the excitation threshold.

[f]Cross section estimated by shifting and scaling the $O_2(^1\Delta)$ cross section by the excitation threshold.

[g]Superelastic cross section calculated using detailed balance for excitation from $O_2(^1\Delta)$.

[h]Cross-section estimated by shifting the ground state cross section by the excitation threshold.

[i]Scaled from O ionization rate expression (Ref. 51) using correlation given by Vriens (Ref. 57).

[j]Estimated.

[k]Rate given by (Ref. 46); assumed branching to ground state.

[l]Rate given by (Ref. 36) with branching given by (Ref. 46).

[m]Rate given by (Ref. 36); assumed half branches to O_2 and half to $O_2(^1\Delta)$.

[n]Estimated same as O_2.

TABLE II. Wall reaction mechanism.

Wall reaction	Reaction probability	Reference
$O_2(v)+\text{wall}\rightarrow O_2$	0.20	
$O_2(^1\Delta)+\text{wall}\rightarrow O_2$	10^{-5}	46
$O_2(^1\Sigma)+\text{wall}\rightarrow O_2$	0.02	46
$O+\text{wall}\rightarrow 1/2\ O_2$	0.02	46
$O(^1D)+\text{wall}\rightarrow O$	1.00	46
$O(^1S)+\text{wall}\rightarrow O$	1.00	46
$He(^2S)+\text{wall}\rightarrow He$	1.00	
$M^+ + \text{wall}\rightarrow M$	1.00	

$$k = 3.0\times 10^{-10}\ \text{cm}^3\ \text{s}^{-1} \quad \text{(Ref. 33)}, \tag{20}$$

$$O + O_2 + M \rightarrow O_3 + O_2 + M,$$

$$k = 6.0\times 10^{-4}\ \text{cm}^6\ \text{s}^{-1} \quad \text{(Ref. 32)}. \tag{21}$$

However, later in the discharge region the $O_2(^1\Sigma)$ density becomes large enough so that the dissociation reaction,

$$O_2(^1\Sigma) + O_3 \rightarrow O + O_2 + O_2,$$

$$k = 7.3\times 10^{-12}\ \text{cm}^3\ \text{s}^{-1} \quad \text{(Ref. 34)}, \tag{22}$$

controls the O_3 density, keeping the O_3 fraction in the ppm range throughout the discharge.

In the early afterglow, there is a brief increase in $O_2(^1\Delta)$ density as the remaining $O_2(^1\Sigma)$ is deexcited by O atoms [Eq. (15)]. The $O_2(^1\Delta)$ metastable has a 64.4 min. radiative lifetime,[35] so high densities persist far downstream in the afterglow. The dominant afterglow reactions reduce the $O_2(^1\Delta)$ density through collisions with O and O_3, and through pooling reactions,

$$O_2(^1\Delta) + O \rightarrow O_2 + O,$$

$$k = 2.0\times 10^{-16}\ \text{cm}^3\ \text{s}^{-1} \quad \text{(Ref. 36)}, \tag{23}$$

$$O_2(^1\Delta) + O_3 \rightarrow O_2 + O_2 + O,$$

$$k = 4.0\times 10^{-15}\ \text{cm}^3\ \text{s}^{-1} \quad \text{(Ref. 37)}, \tag{24}$$

$$O_2(^1\Delta) + O_2(^1\Delta) \rightarrow O_2 + O_2,$$

$$k = 1.4\times 10^{-17}\ \text{cm}^3\ \text{s}^{-1} \quad \text{(Ref. 36)}, \tag{25a}$$

$$O_2(^1\Delta) + O_2(^1\Delta) \rightarrow O_2(^1\Sigma) + O_2,$$

$$k = 1.4\times 10^{-17}\ \text{cm}^3\ \text{s}^{-1} \quad \text{(Ref. 36)}. \tag{25b}$$

Ozone is rapidly depleted immediately after the discharge as its primary source [Eq. (20)] is diminished by O^- recombination. Later in the afterglow, the O_3 density again increases. $O_2(^1\Sigma)$, the dominant quencher of O_3 [Eq. (22)] is depleted by reactions with O atoms [Eq. (15)], thereby allowing the weaker three-body association reaction [Eq. (21)] to repopulate O_3.

A simple wall reaction mechanism describes species diffusing to and returning from the walls. In this mechanism, all ions are neutralized at the wall and return as ground state species. Excited species are quenched on the walls with the probabilities given in Table II, and return to the gas in the ground state. Some of the atomic O reaching the wall recombines to form ground state O_2.

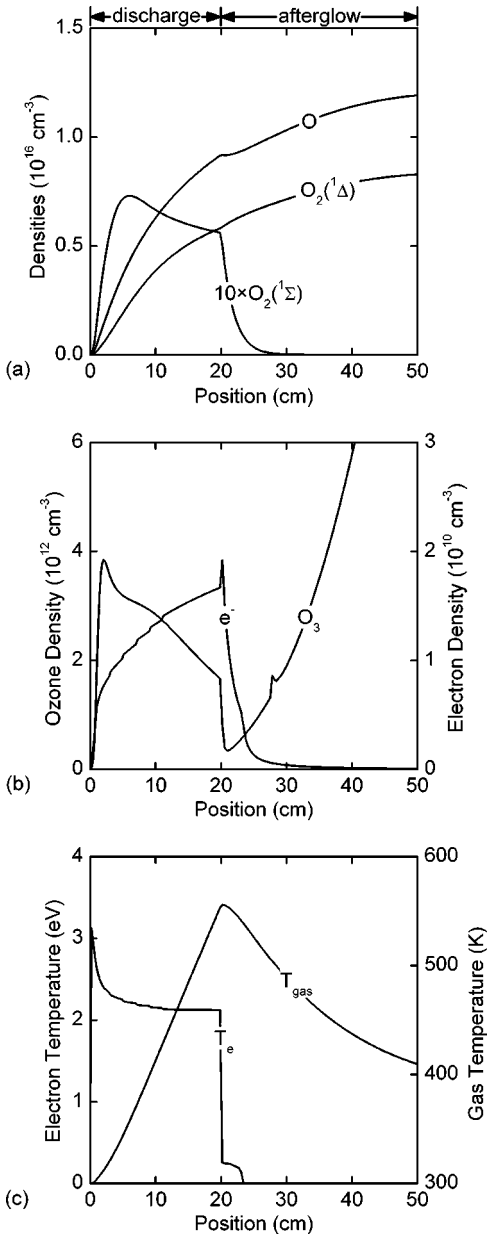

FIG. 2. Plasma properties for the base case (O_2 at 3 Torr, $L=20$ cm, $\nu_{x,in}=1000$ cm/s, $P_{dep}=0.5$ W/cm^3). (a) $O_2(^1\Delta)$, $O_2(^1\Sigma)$, and O atom densities. (b) O_3 and electron densities. (c) Electron and gas temperatures.

GlobalKin has been validated with a similar reaction mechanism for microwave discharges by Zimmerman *et al.*[38] using results from Benard and Pchelkin,[18] and for rf discharges by Carroll *et al.*,[13] using results from capacitive discharges at 2–10 Torr in Ar/He/O_2 mixtures. Good agreement was obtained between the model and experimental results in both cases. Results from GlobalKin using the reaction mechanism discussed in this paper are shown in Fig. 3 with experimental results from Carroll *et al.*[13] The gas temperature was experimentally obtained from the $O_2(^1\Sigma)$ rotational spectra. GlobalKin predicts the gas temperature well despite the simplicity of the radial heat conduction model.

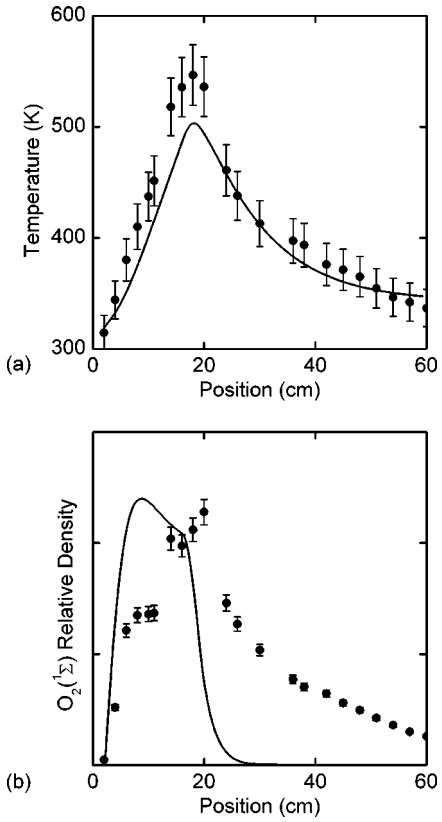

FIG. 3. Comparison of computed results with experiments by Carroll *et al.* for 5 mmol/s of pure O_2 at 2 Torr flowing through a 4.83 cm ID quartz tube (Ref. 13). 265 W was deposited between electrodes spaced 30 cm apart. (a) Gas temperature as a function of position. GlobalKin predicts gas temperature well with a simple heat conduction model. (b) $O_2(^1\Sigma)$ relative density as a function of position.

The predicted peak gas temperature is somewhat lower than the experiment because GlobalKin assumes constant temperature at the discharge tube wall. Due to the difficulty of experimentally obtaining an absolute $O_2(^1\Delta)$ or $O_2(^1\Sigma)$ density, the $O_2(^1\Sigma)$ density from GlobalKin is compared on a relative basis to optical emission sidelight from $O_2(^1\Sigma)$. The fast decay of the $O_2(^1\Sigma)$ density predicted by GlobalKin is markedly different than the slower decay measured in the experiment. The kinetic model developed Savin *et al.* in agreement with their experimental results also predicts a fast decay in $O_2(^1\Sigma)$ density.[16] The rate of decay of $O_2(^1\Sigma)$ in the afterglow is a current topic of discussion.

Comparisons were also made to reported absolute $O_2(^1\Delta)$ densities. The difficulty of experimentally obtaining absolute $O_2(^1\Delta)$ densities is apparent from the broad range of reported $O_2(^1\Delta)$ yields as a function of specific energy. Reported values of $O_2(^1\Delta)$ yield per eV deposited into inlet O_2 molecules range from 0.01 eV^{-1} (Ref. 15) to 0.39 eV^{-1} (Ref. 22) GlobalKin predicts yields between the results reported by Benard and Pchelkin[18] and Savin *et al.*,[16] from 0.06 to 0.08 eV^{-1}. These values are near the median of the results discussed here which correspond to the peak $O_2(^1\Delta)$ yield being at 5–8 eV per molecule of inlet O_2. These scaling will be discussed further below.

There are two definitions of $O_2(^1\Delta)$ yield currently used when discussing COIL systems. The first is the traditional method used when characterizing conventional liquid phase $O_2(^1\Delta)$ generation systems,

$$Y = \frac{[O_2(^1\Delta)]}{[O_2(^3\Sigma)] + [O_2(^1\Delta)]}, \tag{26}$$

where Y is the $O_2(^1\Delta)$ yield and the denominator includes only the ground state $O_2(^3\Sigma)$ and excited $O_2(^1\Delta)$ species. Equation (26) accurately describes $O_2(^1\Delta)$ yields for conventional systems because yields are high and there is little dissociation or excitation to other states.[7] Equation (26) is also convenient when comparing to the threshold yield, which can be derived from Eqs. (1) and (26). However, to describe the $O_2(^1\Delta)$ yield in an electric discharge COIL, dissociation and populated electronic states should be included,

$$Y = \frac{[O_2(^1\Delta)]}{[O_2(^3\Sigma)] + [O_2(v)] + [O_2(^1\Delta)] + [O_2(^1\Sigma)] + 0.5[O] + 1.5[O_3]}. \tag{27}$$

The denominator of Eq. (27) includes all major oxygen species in the discharge on an O_2 equivalent basis, giving the yield Y as the fractional conversion of inlet O_2 to $O_2(^1\Delta)$. The latter method for computing yield [Eq. (27)] was used in this investigation.

IV. SCALING OF $O_2(^1\Delta)$ YIELD

The base case uses conditions similar to experiments performed by others.[20] The electric discharge COIL experiments typically use a 4.83 cm ID Pyrex discharge tube with an axial capacitive or inductive discharge over 20–30 cm of length. Pressures range from a few to tens of Torr, with flow velocities of hundreds to thousands cm/s, giving residence times on the order of a few to tens of milliseconds.[20] Absorbed power in the discharge ranges from tens to hundreds W, corresponding to power depositions from 0.01 to 1 W/cm^3. The base case has a 20 cm discharge length, pure O_2 at 3 Torr, and power deposition of 0.5 W/cm^3.

Densities and temperatures as a function of position are shown in Fig. 2. The $O_2(^1\Delta)$ density rises in the discharge primarily by direct electron impact excitation from ground state O_2 [Eq. (10)], while the O density increases due to dissociation from the ground state [Eqs. (11) and (12)]. The O atom yield on an O_2 equivalent basis is roughly equal to the $O_2(^1\Delta)$ yield for conditions providing peak $O_2(^1\Delta)$ yield (5–8 eV/molecule), giving O densities twice that of the

$O_2(^1\Delta)$ density. (Note that the conditions for Fig. 2 are less than optimum.) The $O_2(^1\Sigma)$ density also initially rises due to electron impact excitation [Eq. (13)], but then plateaus after the O density becomes large enough so that the rate of quenching by O atoms [Eq. (15)] balances the rate of excitation. This is not intrinsically bad as the product of the quenching is dominantly $O_2(^1\Delta)$. Some O_3 is also produced in the discharge region by reaction of O^- and $O_2(^1\Delta)$ [Eq. (20)], but the density also saturates. The source of O_3 changes to $O+O_2$ association as the O density increases and quenching by $O_2(^1\Sigma)$ [Eq. (22)] balances the source. The gas temperature rises nearly 150 K in the pure O_2 discharge, primarily through Frank-Condon heating, which emphasizes the need to cool the gas flow if laser gain is to be achieved.

The electron density quickly rises to 0.6×10^{10} cm^{-3} (at 3 Torr) early in the discharge and then slowly increases to 1.5×10^{10} cm^{-3} by the end of the discharge. The increase in n_e while power is constant is largely due to the dissociation of O_2 and thermal expansion of the gas, both of which reduce the power dissipation (eV/cm^3 s) per electron. The electron density then increases to compensate. The small spike in n_e at the end of the discharge results from loss processes decreasing at a higher rate than ionization processes as T_e decreases. The electron temperature peaks before falling to a stationary value near 2 eV as the electron density saturates.

The initial spike in electron temperature is partly due to the simplicity of the plug flow model, which does not account for upstream electron transport and thus assumes a fairly low electron density (10^5 cm^{-3}) at the beginning of the power deposition envelope. A finite power deposited into a small inventory of electrons requires a large T_e to dissipate. T_e thermalizes quickly at the end of the discharge region. The small knee in the electron temperature at the end of the discharge results from superelastic electron heating, primarily from the vibrational state $O_2(v=1)$ at 0.19 eV. Electron impact excitation is unimportant downstream for these conditions though electron collision quenching persists for another 10–15 cm.

In the afterglow, $O_2(^1\Delta)$ and O densities continue to rise as the gas cools. Conversely, the most important two reaction pathways in the afterglow are $O_2(^1\Delta)$ quenching by O atoms [Eq. (23)] and O_3 formation [Eq. (21)], which reduce the $O_2(^1\Delta)$ and O mole fractions slightly even though the gas density is increasing. Both the $O_2(^1\Delta)$ metastable and the O atom densities persist far downstream, with no appreciable changes in density by 50 cm downstream of the discharge inlet (30 cm from the end of the discharge). The $O_2(^1\Delta)$ yield for this case was 0.108 at the end of the discharge and 0.111 at the end of the flow tube (30 cm downstream of the discharge).

With the goal of maximizing the yield of $O_2(^1\Delta)$, a full factorial experiment was designed to investigate the effects of discharge parameters. The parameters of primary interest for laboratory COIL experiments are pressure, flow velocity, He/O_2 ratio, and power deposition. Other parameters such as the length of the discharge, the discharge tube wall temperature, and the discharge diameter are also of interest, but these were deemed less important than the primary four variables because of their more easily predictable effects.

A four factor, four level full factorial computational experiment (256 cases) was run. Inlet velocities ranged from 500 to 5000 cm/s, total pressures from 1 to 20 Torr, power depositions from 0.1 to 1.5 W/cm^3, and O_2 fractions in He from 0.03 to 1. Although this design allows resolution of linear effects, two-, three-, and four-way interactions, all four variables were expected to have strong interactions that influence $O_2(^1\Delta)$ yield by changing the net amount of energy deposited into the oxygen species. Therefore, the expected four-way interaction of the independent variables was accounted for by defining a new variable, the specific energy deposition $\overline{E_d}$ which, like the yield, is calculated on a molecular oxygen basis,

$$\overline{E_d} = \frac{E_d}{\left[O_2(^3\Sigma)\right] + [O_2(v)] + \left[O_2(^1\Delta)\right] + \left[O_2(^1\Sigma)\right] + 0.5[O] + 1.5[O_3]}, \tag{28}$$

where E_d is the total energy deposited into the gas in eV/cm^3 and $\overline{E_d}$ is the total energy deposited in eV/molecule on an O_2 equivalent basis. Implicit in Eq. (28) is the assumption that little energy is deposited into the He species, which as we show below, is a reasonable assumption for moderate mole fractions of O_2. The choice of values for the independent variables (inlet velocity, pressure, power deposition, and O_2 fraction) results in $\overline{E_d}$ ranging from 0.004 to 265 eV for a 20 cm discharge. Because $\overline{E_d}$ has a much stronger and clearer effect on $O_2(^1\Delta)$ yield than any of the four independent variables taken separately, we propose a scaling law giving the $O_2(^1\Delta)$ yield Y as a function of the specific energy deposition $\overline{E_d}$,

$$Y = f(\overline{E_d}). \tag{29}$$

Results of the full factorial experiment for the scaling of $O_2(^1\Delta)$ and O yields with $\overline{E_d}$ are shown in Fig. 4. The $O_2(^1\Delta)$ yield is at the exit of the discharge region. $O_2(^1\Delta)$ yield increases almost linearly with $\overline{E_d}$ at low specific energy depositions before saturating with yields of $\approx$0.3 by 5–8 eV/molecule. Since the $O_2(^1\Delta)$ state lies at 0.977 eV,

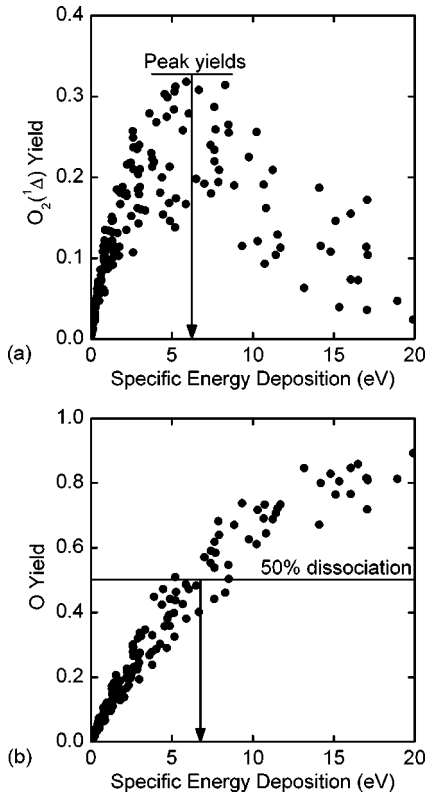

FIG. 4. Yields for a 4 level full factorial design-of-experiments for a 20 cm discharge. (a) $O_2(^1\Delta)$ yields. (b) O yields. The peak $O_2(^1\Delta)$ yield reaches $\approx$0.3 as dissociation reaches 0.5 at $\overline{E_d}$=5–8 eV/molecule.

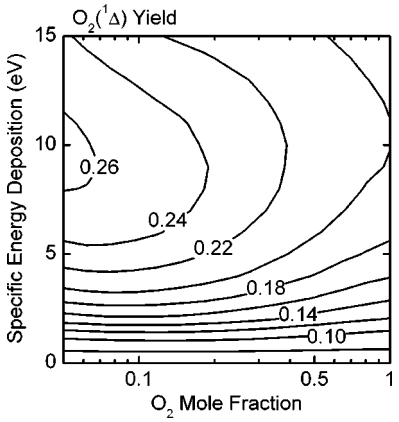

FIG. 5. $O_2(^1\Delta)$ yield as a function of O_2 mole fraction (balance He) and specific energy deposition into O_2 for a constant partial pressure of O_2 of 4.2 Torr, P_d=21 W/cm^3, $\upsilon_{x,in}$=2500 cm/s, and length was varied to obtain the specific energy depositions. The $O_2(^1\Delta)$ yield increases as He is added for parameters near the peak yield ($\overline{E_d}$=5–8 eV).

this corresponds to 0.04–0.06 excitation energy efficiency into $O_2(^1\Delta)$ in the peak yield range of 5–8 eV/molecule.

As more energy is deposited into the oxygen species, dissociation increases [see Fig. 4(b)], reducing the available O_2 that can be excited to $O_2(^1\Delta)$. The depletion of $O_2(^1\Delta)$ by electron impact processes also becomes important. As the $O_2(^1\Delta)$ yield peaks at 5–8 eV/molecule, dissociation into O atoms has reached 50%. O yield continues to monotonically increase as specific energy deposition rises to 20 eV. By 30 eV, almost all of the oxygen is dissociated, and further increases in $\overline{E_d}$ serve only to further excite and ionize the O species. This emphasizes the importance of including O density when discussing $O_2(^1\Delta)$ yields [Eq. (27)]. Although these results show that $O_2(^1\Delta)$ yields follow the scaling law [Eq. (29)], there is a large variation in yields for $\overline{E_d}$ =5–8 eV/molecule, suggesting secondary effects linked to changes in the independent variables. For example, $O_2(^1\Delta)$ yield as a function of energy deposition and O_2 mole fraction is shown in Fig. 5.

The implied E/N as a function of axial position in pure O_2 is shown in Fig. 6(a). The E/N is large at the leading edge of the plasma zone for two major causes. First, the electron density is initially small (10^8 cm^{-3}). Dissipating a finite power by a small inventory of electrons requires a large power dissipation per electron. This is accomplished by having a large T_e which requires a large E/N, as shown in Fig. 2(c). (Analogously, the conductivity is small and so to dissipate a finite power, the electric field must be large.) The large T_e avalanches the plasma, thereby increasing the electron density. As the electron density increases, the power dissipation per electron decreases, thereby requiring a lower T_e and smaller E/N. Second, the gas composition at the leading edge of the plasma zone has few excited states and so electron impact ionization is almost exclusively from ground state species, thereby required a higher T_e and larger E/N. As the excited state inventory builds, the efficiency of ionization increases, thereby requiring a lower T_e and smaller E/N to sustain the plasma.

In electric discharge COIL systems an inert diluent such as He is often added to the O_2 to reduce the temperature rise in the discharge and aid the gas dynamics by increasing the system pressure. The diluent also reduces the amount of flow expansion caused by O_2 dissociation, which in turn increases the residence time in discharge region. The increased residence time leads to higher specific energy deposition with a consequent rise in yield.

When adding He to the discharge at constant O_2 partial pressure (thereby increasing total pressure) and constant specific energy deposition, $O_2(^1\Delta)$ yields can increase, as shown in Fig. 5. At low $\overline{E_d}$, adding He has little effect. In the range of $\overline{E_d}$=5–8 eV/molecule where the yield peaks, adding He can increase the yield several percent. When the He fraction is above $\approx$0.8 more specific energy deposition is required to obtain the peak yield. This additional energy is largely deposited into He through electron momentum transfer collisions. It has been suggested that the addition of an inert diluent such as He may promote higher $O_2(^1\Delta)$ yields by allowing the discharge to operate at a more favorable E/N for $O_2(^1\Delta)$ production.[11,13,20] For our particular conditions the addition of He produces a less favorable E/N than does pure O_2, and a different mechanism is responsible for the increased yields.

Adding He to a O_2 discharge does reduce the quasi-steady-state E/N, as shown in Fig. 6(a). E/N rises rapidly at the discharge inlet to avalanche the low electron density before falling to a quasi-steady-state value, showing the same trend as the electron temperature in Fig. 2(c). The quasi-steady E/N is approached as the rate of ionization balances

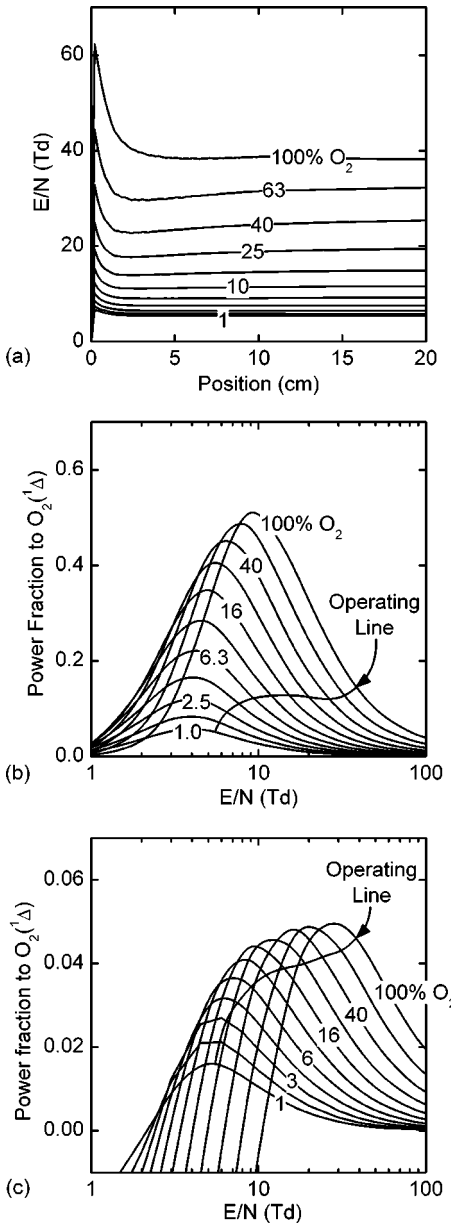

FIG. 6. Effect of diluent on discharge electrodynamics for mixtures of 1%–100% O_2 in He at 3 Torr O_2 partial pressure. (a) E/N for various mixtures as a function of discharge length. (b) Fraction of electron power exciting O_2 to $O_2(^1\Delta)$ as a function of E/N at 0% yield, and (c) 15% yield. The operating line shows where the quasi-steady discharge sustains for each mixture. Electron power spent exciting $O_2(^1\Delta)$ decreases as He addition increases.

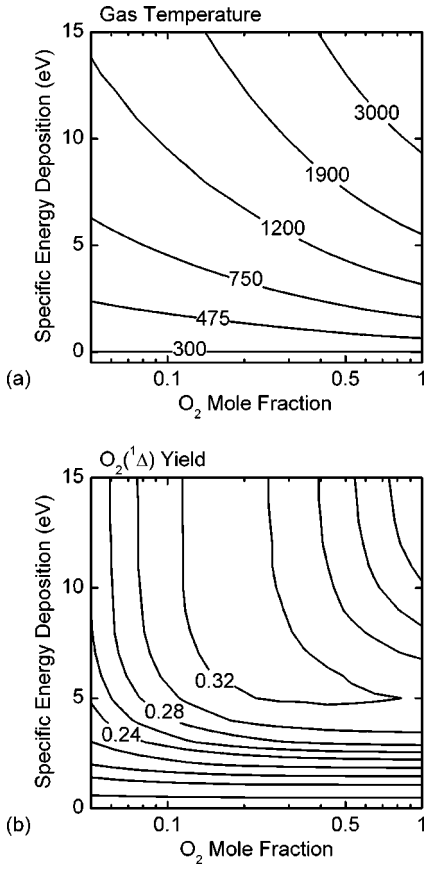

FIG. 7. Effect of He dilution on gas heating. (a) T_g as a function of specific energy deposition and mixture, showing a decrease in gas temperature when O_2 is diluted to 5%. (b) $O_2(^1\Delta)$ yield as a function of O_2 mole fraction and specific energy deposition. The conditions are the same as Fig. 5, except that T_g is fixed at 300 K. The dependence of $O_2(^1\Delta)$ yield on He addition is less pronounced when there is no gas heating.

the rate of loss by diffusion to the walls, attachment, and recombination. The ionization rate exceeds the rate of loss by collisions by the diffusion loss. As such, in the limit of there being no charged particle losses to the walls, the quasi-steady E/N would correspond to a net ionization rate by collisions of zero. The quasi-steady-state E/N predicted by GlobalKin for discharges in pure O_2 at 3 Torr is $\approx$40 Td. Napartovich *et al.* also calculated a quasi-steady value of 40 Td for pure O_2 at 10 Torr using a dc positive column model.[11] For typical He/O_2 ratios near 4/1, the discharge operates from 20 to 30 Td, and E/N falls to below 10 Td for $He/O_2=99/1$. As the O_2 partial pressure is held constant, adding He increases the total pressure. Therefore a portion of the reduction in E/N reflects reduced charged particle loss by diffusion.

In order for the addition of He to increase the yield of $O_2(^1\Delta)$ the fraction of power dissipated in electron impact excitation of $O_2(^1\Delta)$ should increase as E/N decreases. The fraction of power expended in excitation of $O_2(^1\Delta)$ [Eq. (10)] for mixtures of O_2 and He at the inlet conditions is shown in Fig. 6(b). For pure O_2, the maximum power dissipated into $O_2(^1\Delta)$ occurs near 10 Td, but the discharge operates near 40 Td. As He is added, the E/N at which the $O_2(^1\Delta)$ excitation is a maximum decreases as does the operating E/N while the fraction of power dissipated into $O_2(^1\Delta)$ decreases. The reduction in operating E/N made possible by the addition of He does not fully counteract the decrease in the fraction of power dissipated in $O_2(^1\Delta)$ excitation. Therefore, for these conditions the addition of He actually *decreases* the efficiency of electron impact excitation of O_2 to $O_2(^1\Delta)$.

Further along the discharge, after some $O_2(^1\Delta)$ has formed, the net fraction of power to $O_2(^1\Delta)$ by direct electron impact decreases, as the rate of electron quenching collisions with $O_2(^1\Delta)$ through upward excitation [Eq. (16)], dissociation [Eqs. (17) and (18)], and superelastic deexcitation [Eq. (19)] begin to dominate. For example, the fraction of power dissipated in $O_2(^1\Delta)$ excitation after 15% of the inlet O_2 has been converted to $O_2(^1\Delta)$ is shown in Fig. 6(c). In addition to the loss process for $O_2(^1\Delta)$, there is a signifi-

cant density of O at this time which also dissipates power. Below 10 Td, at high He fractions the $O_2(^1\Delta)$ density is high enough that more electron impact events remove power from $O_2(^1\Delta)$ by superelastic collisions [Eq. (19)] than deposit power by direct electron impact, resulting in negative power fractions to $O_2(^1\Delta)$. Sustaining of the $O_2(^1\Delta)$ density at this juncture requires indirect processes such as excitation and subsequent quenching of $O_2(^1\Sigma)$. The fraction of power into $O_2(^1\Delta)$ continues to decrease as the yield increases for self-sustained discharges with He addition, as adding He reduces the rate of direct electron impact.

Inert gases are often added to the discharge to cool the flowing O_2 to make the laser gain kinetics more favorable. The gas cooling also increases the residence time, in turn raising the specific energy deposition at a given power. The higher average gas density also reduces diffusion losses of both excited states and charged particles. The maximum gas temperature is shown in Fig. 7(a) as a function of O_2 mole fraction and $\overline{E_d}$ (O_2 partial pressure is fixed). Due to the increase in heat capacity and thermal conductivity that occurs with He addition, the peak gas temperature decreases with He addition. For example, at $\overline{E_d}$=8 eV, T_g can be reduced to <1000 K with 90% He addition. Although the dominant effect of He addition is to increase the residence time, the gas density also increases relative to the pure O_2 case. Both the reduction in temperature and the net increase in density influence many of the rates in the reaction mechanism, which on the average increases $O_2(^1\Delta)$ yield. For example, $O_2(^1\Delta)$ yield is shown in Fig. 7(b) as a function of O_2 fraction and $\overline{E_d}$ when the gas temperature is held constant at 300 K. Yields are significantly higher than when including the gas dynamics (see Fig. 5), but the dependence on He fraction is less pronounced as the peak yield increases.

The disposition of $O_2(^1\Sigma)$ is an important consideration in determining the ultimate $O_2(^1\Delta)$ yield. In optimistic scenarios the vast majority of $O_2(^1\Sigma)$ can be converted to $O_2(^1\Delta)$ in the downstream region by quenching collisions, principally with O atoms. In this regard we can define an effective yield Y' which includes the contribution of $O_2(^1\Sigma)$:

$$Y' = \frac{[O_2(^1\Delta)] + [O_2(^1\Sigma)]}{[O_2(^3\Sigma)] + [O_2(v)] + [O_2(^1\Delta)] + [O_2(^1\Sigma)] + 0.5[O] + 1.5[O_3]}. \quad (30)$$

Effective yield Y' is shown in Fig. 8(a) for the same conditions as Fig. 5. Up to the value of $\overline{E_d}$ in which peak yield is obtained (5–8 eV/molecule), there is little dependence of yield on mixture. This result suggests that there is a relatively constant dependence of the combined densities of $O_2(^1\Delta)$ and $O_2(^1\Sigma)$ on energy deposition and that the addition of He serves primarily to partition the densities more in favor of $O_2(^1\Delta)$.

To demonstrate this trend, the fraction of total excitation in $O_2(^1\Delta)$,

$$f = \frac{[O_2(^1\Delta)]}{[O_2(^1\Delta)] + [O_2(^1\Sigma)]}, \quad (31)$$

is shown in Fig. 8(b) as a function of O_2 fraction and $\overline{E_d}$ (same conditions as in Fig. 5). There is a 25% increase in the fraction of $O_2(^1\Delta)$ as He dilution increases, corresponding to the 25% increase in raw $O_2(^1\Delta)$ yield shown in Fig. 5. This improvement in $O_2(^1\Delta)$ yield with He addition can be attributed to the decrease in temperature and corresponding rise in density, shifting the ratio of $O_2(^1\Sigma)$ and $O_2(^1\Delta)$ towards a lower value. This is the primary mechanism causing the scatter in yield shown in Fig. 4. As will be discussed below, the improved $O_2(^1\Delta)$ yields at constant $\overline{E_d}$ that result from increasing the total discharge pressure and reducing the power deposition can also be attributed to a shift in the fraction f [Eq. (31)].

The effect of power deposition P_d on $O_2(^1\Delta)$ yield at constant $\overline{E_d}$ and O_2 partial pressure is shown in Fig. 9(a). Peak $O_2(^1\Delta)$ yields are obtained at relatively low power depositions $\leqslant$1 W/cm^3. In simulations of discharges with P_d<0.3 W/cm^3 the electron density did not consistently avalanche, and thus the discharge could not self-sustain. As P_d increases from 0.6 W/cm^3 (peak yield) to 30 W/cm^3 the yield roughly halves and is nearly independent of He addition. However, varying P_d has a smaller effect on the effective yield Y', as shown in Fig. 9(b). Although the peak still occurs at relatively low power depositions, Y' decreases just 5% when P_d is increased to 30 W/cm^3. The cause for this result, as shown in Fig. 9(c), is that the fraction f of excited $O_2(^1\Delta)$ roughly halves when P_d is increased from 0.6 to 30 W/cm^3, which largely replicates the same trend as for the $O_2(^1\Delta)$ yield. Therefore, as with He addition, the increase in $O_2(^1\Delta)$ yield as P_d decreases is primarily caused not by a change in E/N, but by a shift in the $O_2(^1\Sigma)$ disposition in favor of $O_2(^1\Delta)$. Operation at lower power depositions requires longer discharge lengths (longer residence times) to reach the $\overline{E_d}$ at which peak yield is obtained (5–8 eV/molecule), allowing for more efficient heat transfer. This leads to lower gas temperatures and higher species densities, reducing the $[O_2(^1\Sigma)]/[O_2(^1\Delta)]$ ratio and increasing the $O_2(^1\Delta)$ yield.

Discharge operation at the lower power depositions at which $O_2(^1\Delta)$ yields are optimized requires longer discharge lengths than are typically used in COIL experiments. The power deposition selected for the discharge is ultimately a function of the desired $O_2(^1\Delta)$ yield Y and the gas flow rate. To optimize the $O_2(^1\Delta)$ yield, $\overline{E_d}$ should be

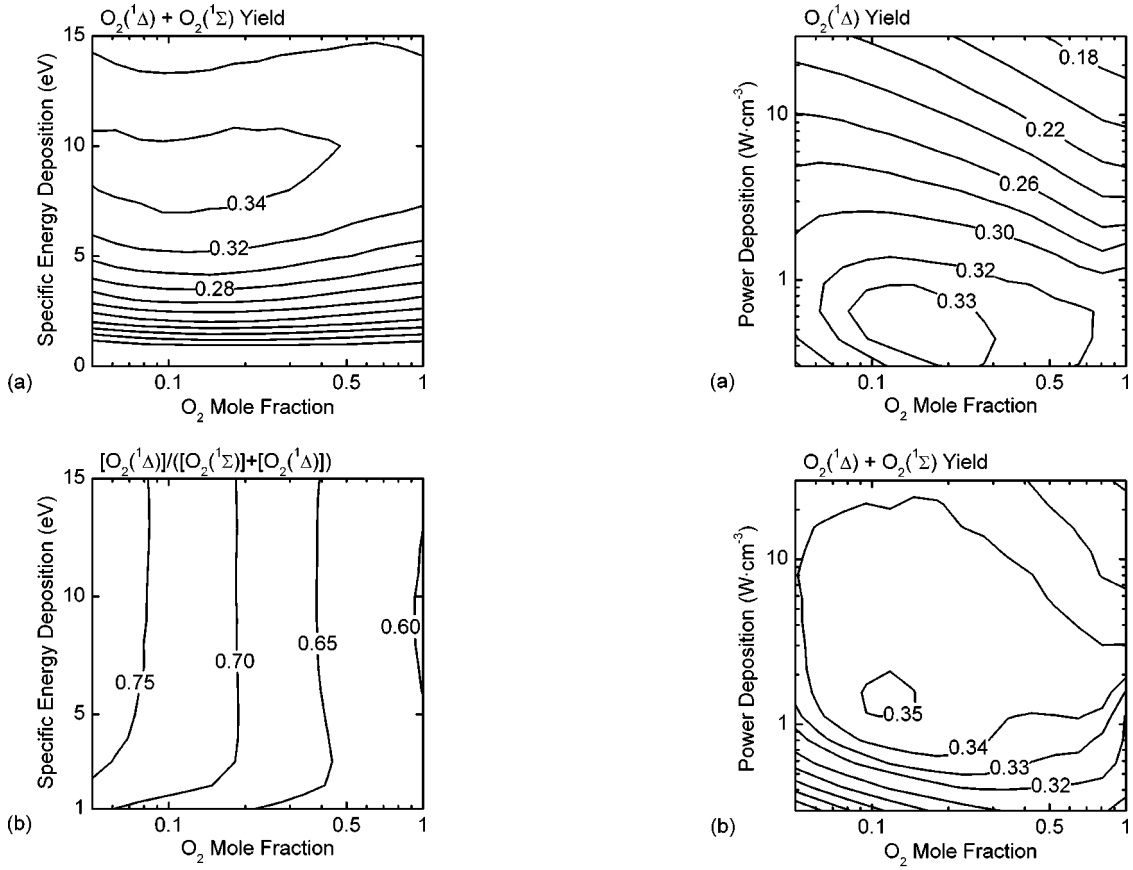

FIG. 8. Effect of $[O_2(^1\Sigma)]/[O_2(^1\Delta)]$ partition on $O_2(^1\Delta)$ yield. (a) Effective yield Y' of $O_2(^1\Sigma)+O_2(^1\Delta)$ as a function of specific energy deposition and mixture. (b) $f=[O_2(^1\Delta)]/([O_2(^1\Delta)]+[O_2(^1\Sigma)])$ as a function of specific energy deposition and mixture. Conditions are the same as in Fig. 5. The fraction of $O_2(^1\Delta)$ increases as He is added to the discharge, causing the $O_2(^1\Delta)$ yield to increase, but the effective yield Y' is relatively unaffected.

FIG. 9. Yields as a function of power deposition and O_2 mole fraction for $\overline{E_d}=8$ eV/molecule and O_2 partial pressure of 3 Torr. (a) $O_2(^1\Delta)$ yield Y. (b) $O_2(^1\Delta)$ and $O_2(^1\Sigma)$ combined yield Y'. (c) $O_2(^1\Delta)$ fraction f. $O_2(^1\Delta)$ yield and fraction are higher at low P_d because more $O_2(^1\Sigma)$ has been converted to $O_2(^1\Delta)$, but the combined yield is relatively constant from 1 to 10 W/cm^3.

5–8 eV/molecule. For a typical discharge in a $He/O_2=90/10$ mixture at 30 Torr flowing at 3000 cm/s the residence time in the 30 cm discharge region is 10 ms. Thus, 500–800 eV/s molecule must be deposited into O_2 species, corresponding to 8–12 W/cm^3 at an O_2 partial pressure of 3 Torr. This value of P_d is well above that which optimizes $O_2(^1\Delta)$ yield, as shown in Fig. 9(a). For comparable $\overline{E_d}$ at low power depositions, a much longer discharge is required. For example, for $P_d=0.6$ W/cm^3 [in the peak $O_2(^1\Delta)$ yield zone] the discharge length would need to be 4–6 m to reach $\overline{E_d}=5$–8 eV/molecule—an order of magnitude longer than the 10–30 cm discharge lengths of current experiments.[15,16,21]

When the specific energy deposition $\overline{E_d}$ and the power deposition P_d are optimized and the discharge is operating near peak yield, varying the total pressure has little effect on the $O_2(^1\Delta)$ yield. $O_2(^1\Delta)$ yield Y is shown as a function of the total pressure and O_2 mole fraction in Fig. 10(a) for $\overline{E_d}=8$ eV and $P_d=1$ W/cm^3 Torr O_2. For moderate total pressures above 20 Torr, the $O_2(^1\Delta)$ yield is nearly independent of pressure. The effective yield Y' is also nearly independent of pressure above 20 Torr, as shown in Fig. 10(b). The small dependence of Y' on pressure is due to the already small $[O_2(^1\Sigma)]/[O_2(^1\Delta)]$ ratio for these conditions. Near the peak values ($Y\approx 0.31, Y'\approx 0.35$), the $[O_2(^1\Sigma)]/[O_2(^1\Delta)]$ ratio is ≈ 0.13.

To summarize the secondary effects of He addition, power deposition, and pressure, the effective yield Y' is shown in Fig. 11 for the same full factorial experiment of Fig. 4. The raw $O_2(^1\Delta)$ yield has >50% variation at a given $\overline{E_d}$ near its peak value (5–8 eV/molecule), but the effective yield $[O_2(^1\Delta)+O_2(^1\Sigma)]$ has <20% variation at the same $\overline{E_d}$. Since most of the $O_2(^1\Sigma)$ generated in the discharge is con-

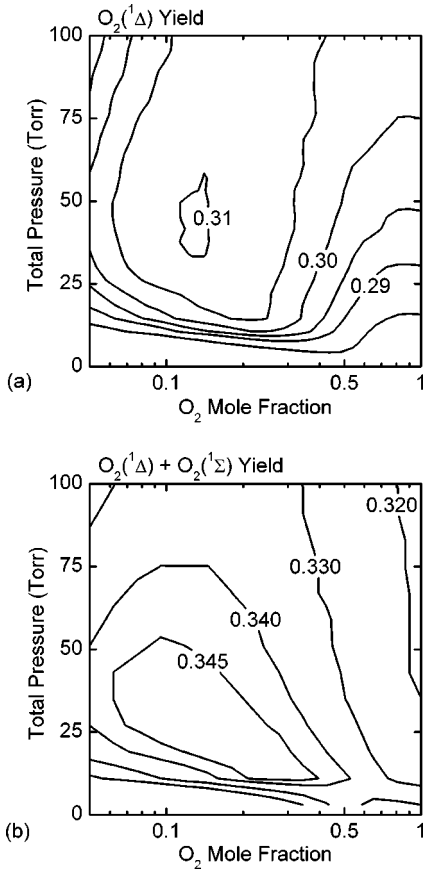

FIG. 10. $O_2(^1\Delta)$ yields at $\bar{E}_d$=8 eV/molecule as a function of total pressure and O_2 mole fraction at a P_d of 3 W/cm^{3}Torr O_2. (a) $O_2(^1\Delta)$ yield Y. (b) $O_2(^1\Delta)$ and $O_2(^1\Sigma)$ combined yield Y'. When $\bar{E}_d$ and P_d have been optimized, neither Y nor Y' are strong functions of total pressure above 20 Torr.

verted to $O_2(^1\Delta)$ in the near afterglow, Y' is likely a better indicator for COIL discharge performance. In this regard, $O_2(^1\Delta)$ production for typical flowing COIL conditions is almost exclusively a function of specific energy deposition into the oxygen species, and is nearly independent of He addition, power deposition, and pressure if enough energy (5–8 eV/molecule) is deposited.

In the context of the effective yield Y' the reaction mechanism can be conceptually simplified to five classes of

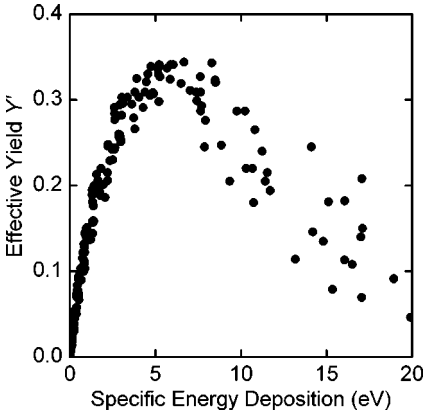

FIG. 11. Effective yield Y' for same conditions as Fig. 4. At fixed $\bar{E}_d$ in the peak effective yield regime (5–8 eV/molecule), there is less scatter than for the $O_2(^1\Delta)$ yield Y [Fig. 4(a)].

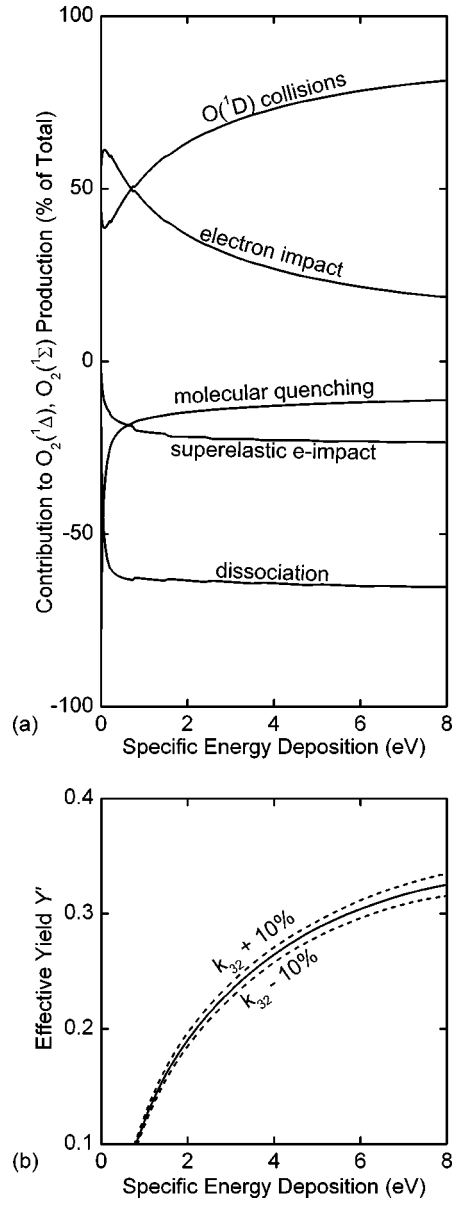

FIG. 12. Importance of classes of reactions as a function of specific energy deposition $\bar{E}_d$ in pure O_2. (a) $O_2(^1\Delta)$ and $O_2(^1\Sigma)$ production or loss processes as a percentage of the total production rate. (b) Sensitivity of the effective yield Y' to ±10% uncertainty in k_{32}. Conditions are the same as in Fig. 5. As $\bar{E}_d$ increases later in the discharge, $O(^1D)$ collisions dominate $O_2(^1\Delta)$ production. At $\bar{E}_d$=8 eV/molecule, $O(^1D)$ reactions also account for most of the sensitivity in the model, where ±10% variation in k_{32} causes ±1% variation in Y'.

processes which either generate or deplete $O_2(^1\Delta)$ and $O_2(^1\Sigma)$. The classes of production reactions are direct electron impact from the ground state and excitation transfer from $O(^1D)$. The classes of loss processes are quenching by collisions with molecules, superelastic electron collisions and electron impact dissociation. The fractional contributions of these processes for a discharge in pure O_2 are shown in Fig 12(a) as a function of energy deposition.

As $\bar{E}_d$ increases, dissociation becomes more important. O atoms generated by dissociation are excited to $O(^1D)$ through electron impact [Eq. (32)] and then excite ground state O_2 to $O_2(^1\Sigma)$ [Eq. (14)]. Excitation transfer from $O(^1D)$

becomes the most important source of $O_2(^1\Delta)$ and $O_2(^1\Sigma)$ at higher $\overline{E_d}$. Electron impact excitation of ground state O_2 decreases as $\overline{E_d}$ increases and O_2 is depleted [Eqs. (10) and (13)]. Superelastic electron impact and molecular quenching reactions are secondary loss mechanisms, making up less than 40% of the losses at $\overline{E_d} \geqslant 1$ eV/molecule.

The sensitivity of results from the model to the values of rate coefficients for the reactions in Table I was determined by individually varying the rate coefficients in a sensitivity analysis. When the individual rate coefficients were changed by ±10%, only four reactions caused variation ⩾1% in Y'. These four reactions are the primary reactions influencing the effective yield in high yield discharges and are repeated here in order of decreasing model sensitivity:

$$e + O \rightarrow O(^1D) + e, \tag{32}$$

$$O(^1D) + O_2 \rightarrow O + O_2(^1\Sigma), \tag{14'}$$

$$e + O_2 \rightarrow O_2(^1\Delta) + e, \tag{10'}$$

$$O(^1D) + O \rightarrow O + O. \tag{33}$$

A full factorial sensitivity analysis showed that the two-, three-, and four-way interactions between variations in the rate coefficients of these four reactions were insignificant compared to their individual (first-order) effects. The sensitivity of Y' to individual variations in these four reaction rate coefficients is +10%, +7%, +5%, and −5%. For example, increasing the most sensitive rate coefficient, k_{32} [Eq. (32)], by +10% changes the effective yield Y' by only +1%.

Predicted yields obtained by varying $k_{32} \pm 10\%$ from its default value are shown in Fig. 12(b). Even at $\overline{E_d} = 8$ eV/molecule, the effective yield is relatively insensitive to reasonable uncertainties in k_{32}. Y' ranged from 31 to 33%, when k_{32} was varied ±10%. It is therefore unlikely that reasonable uncertainties in the rate coefficients will significantly change our qualitative conclusions; however, there may be systematic quantitative changes. It is important to note that there are physical phenomena that are not captured by the pseudo-plug-flow model which may limit the optimum yields predicted here. Some of these processes are axial diffusive transport of mass and energy and discharge instabilities such as constriction and striations.

V. CONCLUDING REMARKS

The gas phase kinetics of flowing He/O_2 discharges used in COIL systems have been investigated. Using a modified global plasma kinetics model to simulate the plug flow, the effects of velocity, pressure, power deposition, and He addition on the $O_2(^1\Delta)$ yield were investigated. The $O_2(^1\Delta)$ yield was found to scale principally with specific energy deposition into oxygen species. Increasing the specific energy deposition increases the $O_2(^1\Delta)$ yield up to a peak value of ≈0.3 near $\overline{E_d} = 5-8$ eV/molecule. At a constant specific energy deposition near peak yield, adding He, reducing the power deposition, and increasing the pressure increases the $O_2(^1\Delta)$ yield to lesser extent than specific energy deposition. Although these secondary effects increase $O_2(^1\Delta)$ yield in the discharge, they have little effect on the combined $O_2(^1\Delta)$ and $O_2(^1\Sigma)$ yield. Since most of the $O_2(^1\Sigma)$ is converted to $O_2(^1\Delta)$ in the early afterglow, the discharge performance for COIL systems will likely be determined by specific energy deposition.

ACKNOWLEDGEMENTS

This work was supported by the Air Force Research Labs, the Air Force Office of Scientific Research, and the National Science Foundation (Grant Nos. CTS 99-74962, CTS 03-15353). The authors thank W. Solomon, J. Zimmerman, D. Carroll, and J. Verdeyen of CU-Aerospace; and T. Madden and G. Hager of the Air Force Research Lab for their insights into the operation of COILs.

[1] W. E. McDermott, N. R. Pchelkin, D. J. Benard, and R. R. Bousek, Appl. Phys. Lett. **32**, 469 (1978).
[2] H. Fujii, S. Yoshida, M. Iizuka, and T. Atsuta, J. Appl. Phys. **67**, 3948 (1990).
[3] A. Elior, B. D. Barmashenko, E. Lebiush, and S. Rosenwaks, Appl. Phys. B: Lasers Opt. **61**, 37 (1995).
[4] M. Endo *et al.*, IEEE J. Quantum Electron. **34**, 393 (1998).
[5] D. Furman, E. Bruins, V. Rybalkin, B. D. Barmashenko, and S. Rosenwaks, IEEE J. Quantum Electron. **37**, 174 (2001).
[6] J. Kodymova, O. Spalek, V. Jirasek, M. Censky, and G. D. Hager, Appl. Phys. A: Mater. Sci. Process. **77**, 331 (2003).
[7] J. Kodymova and O. Spalek, Jpn. J. Appl. Phys., Part 1 **37**, 117 (1998).
[8] D. L. Carroll and W. C. Solomon, *ElectriCOIL: An Advanced Chemical Iodine Laser Concept*, Proceedings of the XIII International Symposium on Gas Flow and Chemical Lasers and High Power Laser Conference, Florence, Italy, 18–22 September 2000, edited by A.Lapucci (SPIE, Bellingham, p. 40.
[9] T. L. Henshaw, T. J. Madden, G. C. Manke, B. T. Anderson, R. F. Tate, M. R. Berman, and G. D. Hager, AIAA Pap. (2000).
[10] A. Hill, *The next generation of controlled avalanche discharge gas lasers*, International Conference on Lasers, Albuquerque, NM, 2000 (STS, McLean, VA 2000).
[11] A. P. Napartovich, A. Deryugin, and I. Kochetov, J. Phys. D **34**, 1827 (2001).
[12] J. Schmiedberger and H. Fujii, Appl. Phys. Lett. **78**, 2649 (2001).
[13] D. L. Carroll, D. M. King, J. T. Verdeyen, B. Woodard, J. W. Zimmerman, L. Skorski, and W. C. Solomon, AIAA Pap. (2003).
[14] A. A. Ionin, Y. M. Klimachev, A. A. Kotkov, I. V. Kochetov, A. P. Napartovich, L. V. Seleznev, D. V. Sinitsyn, and G. D. Hager, J. Phys. D **36**, 982 (2003).
[15] T. V. Rakhimova *et al.*, AIAA Pap. (2003).
[16] Y. V. Savin *et al.*, AIAA Pap. (2003).
[17] J. F. Hon, D. N. Plummer, P. G. Crowell, J. Erkkila, G. D. Hager, C. A. Helms, and K. A. Truesdell, AIAA Pap. (1994).
[18] D. J. Benard and N. R. Pchelkin, Rev. Sci. Instrum. **49**, 794 (1978).
[19] G. Fournier, J. Bonnet, D. David, and D. Pigache, *Excitation of singlet oxygen at atmospheric pressure*, Proceedings of Phenomena in Ionized Gases II, Minsk, 1981, p. 837.
[20] D. M. King, D. L. Carroll, J. K. Laystrom, J. T. Verdeyen, M. S. Sexauer, and W. C. Solomon, *ElectriCOIL: Preliminary Experiments of Excited Oxygen Generation by RF Discharge*, Proceedings of the International Conference on Lasers Albuquerque, NM, 2000 (STS, McLean, VA, 2001) p. 265.
[21] D. L. Carroll, J. T. Verdeyen, J. W. Zimmerman, L. Skorski, and W. C. Solomon, AIAA Pap. (2003).
[22] J. T. Verdeyen, D. M. King, D. L. Carroll, and W. C. Solomon, *Diagnostic development for the ElectriCOIL flow system*, Proceedings of the Gas and Chemical Lasers and Intense Beam Applications III Conference, San Jose, CA, 22–24 January 2002, 2002 (SPIE) edited by (S. Davis, and M. Heaven (SPIE, Bellingham, 2002) p. 154.
[23] D. L. Carroll, J. T. Verdeyen, D. M. King, B. Woodard, L. Skorski, J. W. Zimmerman, and W. C. Solomon, *Recent Work on the Development of an Electric Discharge Oxygen Iodine Laser*, XIVInternational Symposium on Gas Flow and Chemical Lasers and High Power Laser Conference, Wro-

claw, Poland, 2002 edited by K. Abramski, E. Plinski, and W. Wolinski (SPIE, Bellingham, 2002).
[24]R. Dorai, K. Hassouni, and M. J. Kushner, J. Appl. Phys. **88**, 6060 (2000).
[25]P. N. Brown, G. D. Byrne, and A. C. Hindmarsh, SIAM (Soc. Ind. Appl. Math.) J. Sci. Stat. Comput. **10**, 1038 (1989).
[26]H. W. Ellis, E. W. McDaniel, D. L. Albritton, L. A. Viehland, S. L. Lin, and E. A. Mason, At. Data Nucl. Data Tables **22**, 179 (1978).
[27]H. W. Ellis, R. Y. Pai, E. W. McDaniel, E. A. Mason, and L. A. Viehland, At. Data Nucl. Data Tables **17**, 177 (1976).
[28]H. W. Ellis, M. G. Thackston, E. W. McDaniel, and E. A. Mason, At. Data Nucl. Data Tables **31**, 113 (1984).
[29]L. A. Viehland and E. A. Mason, At. Data Nucl. Data Tables **60**, 37 (1995).
[30]R. M. Felder and R. W. Rousseau, *Elementary Principles of Chemical Processes* (Wiley, New York, 1999).
[31]S. D. Rockwood, Phys. Rev. A **8**, 2348 (1973).
[32]R. Atkinson, D. L. Baulch, R. A. Cox, J. R. F. Hampson, J. A. Kerr, M. J. Rossi, and J. Troe, J. Phys. Chem. Ref. Data **26**, 521 (1997).
[33]Y. Ikezoe, S. Matsuoka, M. Takebe, and A. Viggiano, *Gas Phase Ion-Molecule Reaction Rate Constants Through 1986* (Ion Reaction Research Group of the Mass Spectroscopy Society of Japan, Tokyo, Japan, 1987).
[34]K. W. Choo and M. T. Leu, Int. J. Chem. Kinet. **17**, 1155 (1985).
[35]S. M. Newman, A. J. Orr-Ewing, D. A. Newnham, and J. Ballard, J. Phys. Chem. A **104**, 9467 (2000).
[36]J. T. Herron and D. S. Green, Plasma Chem. Plasma Process. **21**, 459 (2001).
[37]R. Atkinson, D. L. Baulch, R. A. Cox, J. R. F. Hampson, J. A. Kerr, M. J. Rossi, and J. Troe, J. Phys. Chem. Ref. Data **26**, 1329 (1997).
[38]J. W. Zimmerman, L. W. Skorski, W. C. Solomon, M. J. Kushner, J. T. Verdeyen, and D. L. Carroll, *Electrodynamic modeling of the ElectriCOIL system*, LASE 2003 Conference, San Jose, California, 2003 (SPIE) edited by S. Davis and M. Heaven(SPIE, Bellingham, 2003), p. 81.
[39]J. P. Boeuf and E. Marode, J. Phys. D **15**, 2169 (1982).
[40]D. Rapp and P. Englander-Golden, J. Chem. Phys. **43**, 1464 (1965).
[41]L. Vriens, Phys. Lett. **8**, 260 (1964).
[42]G. Bekefi, *Radiation Processes in Plasmas* (Wiley, New York, 1966).
[43]A. V. Phelps, JILA Information Center Report No. 28, 1985.
[44]E. Krishnakumar and S. K. Srivastava, Int. J. Mass Spectrom. Ion Processes **113**, 1 (1992).
[45]Y. Itikawa *et al.*, J. Phys. Chem. Ref. Data **18**, 23 (1989).
[46]B. F. Gordiets, C. M. Ferreira, V. L. Guerra, J. Loureiro, J. Nahorny, D. Pagnon, M. Touzeau, and M. Vialle, IEEE Trans. Plasma Sci. **23**, 750 (1995).
[47]P. D. Burrow, J. Chem. Phys. **59**, 4922 (1973).
[48]R. I. Hall and S. Trajmar, J. Phys. B **8**, L293 (1975).
[49]S. Matejcik *et al.*, Plasma Sources Sci. Technol. **6**, 140 (1997).
[50]R. R. Laher and F. R. Gilmore, J. Phys. Chem. Ref. Data **19**, 277 (1990).
[51]E. Meeks, R. S. Larson, P. Ho, C. Apblett, S. M. Han, E. Edelberg, and E. S. Aydil, J. Vac. Sci. Technol. A **16**, 544 (1998).
[52]J. Shi and J. R. Barker, Int. J. Chem. Kinet. **22**, 1283 (1990).
[53]*NIST Standard Reference Database 17-2Q98* (National Institute of Standards and Technology, Gaithersburg, MD, 1998).
[54]B. Eliasson and U. Kogelschatz, Brown Boveri Technical Report LKR 86-11 C, 1986.
[55]R. Deloche, P. Monchicourt, M. Cheret, and F. Lambert, Phys. Rev. A **13**, 1140 (1976).
[56]J. M. Pouvesle, A. Khacef, J. Stevefelt, H. Jahani, V. T. Gylys, and C. B. Collins, J. Chem. Phys. **88**, 3061 (1988).
[57]L. Vriens, Phys. Rev. **141**, 88 (1966).